Assimilation of Precipitation-Affected Radiances in a Cloud-Resolving WRF Ensemble Data Assimilation System

SARA Q. ZHANG

NASA Goddard Space Flight Center, Greenbelt, Maryland

MILIJA ZUPANSKI

Cooperative Institute for Research in the Atmosphere, Colorado State University, Fort Collins, Colorado

ARTHUR Y. HOU AND XIN LIN

NASA Goddard Space Flight Center, Greenbelt, Maryland

SAMSON H. CHEUNG

University of California, Davis, Davis, California

(Manuscript received 16 February 2012, in final form 17 September 2012)

ABSTRACT

Assimilation of remotely sensed precipitation observations into numerical weather prediction models can improve precipitation forecasts and extend prediction capabilities in hydrological applications. This paper presents a new regional ensemble data assimilation system that assimilates precipitation-affected microwave radiances into the Weather Research and Forecasting Model (WRF). To meet the challenges in satellite data assimilation involving cloud and precipitation processes, hydrometeors produced by the cloud-resolving model are included as control variables and ensemble forecasts are used to estimate flow-dependent background error covariance. Two assimilation experiments have been conducted using precipitation-affected radiances from passive microwave sensors: one for a tropical storm after landfall and the other for a heavy rain event in the southeastern United States. The experiments examined the propagation of information in observed radiances via flow-dependent background error auto- and cross covariance, as well as the error statistics of observational radiance. The results show that ensemble assimilation of precipitation-affected radiances improves the quality of precipitation analyses in terms of spatial distribution and intensity in accumulated surface rainfall, as verified by independent ground-based precipitation observations.

1. Introduction

Precipitation is a crucial component in the hydrological cycle of the earth and has a profound influence on the weather and climate at global and regional scales. In recent decades observations of precipitation with global coverage have become available from spaceborne instruments. Spaceborne microwave sensors have the capability to observe precipitation via interaction of hydrometeors in the atmosphere with the radiation field. Following the success of the Tropical Rainfall Measuring Mission (TRMM; Simpson et al. 1996), the Global Precipitation Measurement (GPM) mission, led by the National Aeronautics and Space Administration (NASA) and the Japan Aerospace Exploration Agency (JAXA), will be launched in 2014 and provide the next generation of precipitation observations from a constellation of research and operational microwave sensors covering all parts of the world every 2–4 h (Hou et al. 2008).

With the vast amount of satellite precipitation observations becoming available, it is important to make effective use of these data in numerical weather prediction (NWP) and hydrological applications to improve the quality of model precipitation analyses and forecasts. However, the assimilation of precipitation observations into the NWP system has significant challenges.

Corresponding author address: Sara Q. Zhang, NASA Goddard Space Flight Center, Code 612, Greenbelt, MD 20771.
E-mail: sara.q.zhang@nasa.gov

DOI: 10.1175/MWR-D-12-00055.1

© 2013 American Meteorological Society

In operational global or regional data assimilation systems, satellite observations in cloudy and precipitating regions are often not used due to difficulties that arise when incorporating complex cloud and precipitation processes into data assimilation algorithms. Data assimilation is an estimation procedure of combining information from model forecasts, observations, and statistical descriptions of their uncertainties. When cloud and precipitation are present, model forecasts have errors with large variability in spatial and temporal scales, and remotely sensed observations have more complicated nonlinear sensitivity to model state variables. For instance, a variational assimilation algorithm such as three- or four-dimensional variational data assimilation (3DVAR or 4DVAR) requires a tangent linear model and its adjoint for nonlinear moist physics parameterization and radiative transfer with the presence of hydrometeors. Since cloud and precipitation processes have a flow-dependent nonlinear relationship to the model state variables in NWP, even careful linearization and simplification to the model physics parameterization may sometimes fail to yield an optimal solution for solving the analysis equation, as discussed in Lopez (2007) and Errico et al. (2007). In practice, operational systems have adopted various pragmatic strategies such as strict data quality control and relinearization of nonlinear model physics between low-resolution minimizations (Bauer et al. 2010). Furthermore, a background error covariance needs to adequately characterize errors associated with cloud and precipitation processes. But precipitation and clouds are inherently highly variable in space and time. It is difficult to represent their error distributions with a prescribed static and isotropic background error covariance, as has been commonly used in operational variational analyses. Montmerle and Berre (2010) used an ensemble-based method to investigate the variations of background error covariance between precipitating and nonprecipitating regions, and introduced a two-term approach for a heterogeneous background error covariance with specific error representations for precipitating areas. When considering all-sky radiance assimilation, clouds and precipitation also cause larger discrepancies between model-simulated and observed radiances, particularly where the forecast and observations disagree over clear- or cloudy-sky conditions (Geer and Bauer 2011).

Over the last decade, various approaches have been developed and tested. Retrieved surface rain rates from satellite observations have been assimilated into the National Centers for Environment Prediction (NCEP) 3DVAR system (Treadon et al. 2002). Global precipitation analyses have been produced by assimilating satellite rainfall retrievals into the Goddard Earth Observing System (GEOS) global Data Assimilation System (DAS) using a variational methodology with the model moist physics as a weak constraint (Hou et al. 2004; Hou and Zhang 2007). The European Centre for Medium-Range Weather Forecasts (ECMWF) pioneered the direct assimilation of microwave radiance affected by precipitation, first in a 1 + 4DVAR assimilation approach (Bauer et al. 2006a,b) and, later, in an implementation of all-sky radiance assimilation in the operational 4DVAR system (Bauer et al. 2010; Geer et al. 2010).

With the increase in computational power in recent decades, there have been considerable research activities in ensemble data assimilation techniques and high-resolution numerical modeling. Significant progress has been made in the development and tests on ensemble data assimilation systems. At global scales, ensemble Kalman filter schemes have been developed and tested with operational NWP systems using real atmospheric observations (Buehner et al. 2010a,b; Whitaker et al. 2008; Tong and Xue 2008a,b). At mesoscales, Meng and Zhang (2008) developed an ensemble Kalman filter for mesoscale data assimilation and conducted performance comparisons to a 3DVAR system. Dowell et al. (2011) assimilated ground-based radar reflectivity observations in an ensemble Kalman filter to investigate the bias errors in predicted rain mixing ratio and size distribution from microphysics in the prediction model. Their assimilation experiment of a city supercell also demonstrated a positive data impact on the storm-scale analysis. New developments at major operational centers have incorporated ensemble assimilation methodologies, such as a hybrid variational-ensemble data assimilation scheme at NCEP (Kleist 2010) and an ensemble of low-resolution 4DVAR data assimilation systems being introduced at ECMWF (Isaksen et al. 2010). However, most of the development and progress have been limited to using clear-sky radiance and conventional data, or all-sky radiances over ocean surfaces only. Little progress has been reported in using radiance observations under cloudy and precipitating conditions over land, where improvement is particularly needed for hydrological applications.

The immediate appeal of ensemble methods for precipitation assimilation is that the flow-dependent error covariance dynamically reflects the up-to-date occurrence of rain events and storms, and the ensemble of nonlinear forward model operations projects information between control variables and observables for precipitation processes. To test the feasibility of using an ensemble approach for assimilating cloud and precipitation observations at cloud-resolving scales, a prototype ensemble assimilation system using Weather Research

and Forecasting Model (WRF) has been developed to downscale satellite precipitation data, as previously reported in Zupanski et al. (2011). In this paper we present further details of the NASA regional WRF Ensemble Data Assimilation System (WRF-EDAS) and experimental results of assimilating spaceborne observations of precipitation. For the first time since utilizing direct assimilation of precipitation-affected radiance into a high-resolution NWP system, several new approaches are developed in the WRF-EDAS: (i) flow-dependent background error covariance, (ii) a nonlinear cloud physics and all-sky radiative transfer to link the control variables and observations, (iii) prognostic hydrometeors from cloud-resolving model physics as a part of the control variables in addition to dynamical variables, and (iv) spaceborne observations of precipitation over land. The ultimate aim of this research is to bring together the information from cloud-resolving model simulations and observations from multiple platforms to produce a dynamically consistent precipitation analysis at the scale suitable for hydrological applications.

In the following sections we give an overview on the system configuration and the assimilation algorithm. We present two assimilation experiments using precipitation-affected radiance data over land: a case from Tropical Storm Erin, to examine the estimation of flow-dependent background error covariance, and a case from a southeastern U.S. heavy rain event, to investigate error statistics in observational radiance space and to evaluate the system's performance in bringing observation impact to precipitation forecasts. The last section gives conclusions and future research directions.

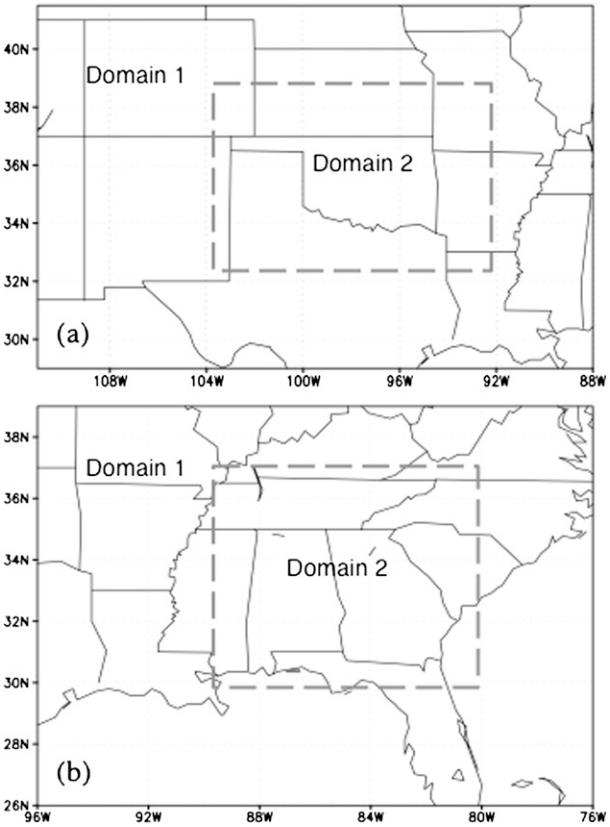

FIG. 1. WRF domain configurations: (a) Tropical Storm Erin and (b) the southeastern U.S. heavy rain event. Resolutions are at 9 and 3 km for the outer and inner domains, respectively.

2. System overview

The NASA regional WRF-EDAS is an ensemble assimilation system designed to assimilate precipitation-affected radiances along with conventional observations into WRF at cloud-resolving scales. A prototype of the system described in Zupanski et al. (2011) provides the baseline for the current system configuration.

The Advanced Research core of the WRF (ARW) with the microphysics schemes of the Goddard Cumulus Ensemble (Tao 2003; Zeng et al. 2008) provides ensemble forecasts for the flow-dependent background covariance estimation and the first-guess fields. The model domains can be configured as nested grids with decreasing horizontal resolutions. Figure 1 shows the model domain configurations that are used in the two assimilation experiments. There are 31 vertical levels and the top level is set at 50 hPa. An ensemble of forecasts is constructed by applying perturbations to the model state variables at the initial time of the WRF 3-h forecasts. The perturbations are generated according to the error statistical characteristics described by the analysis error covariance. Parameters at lateral domain boundaries and at the land surface are unperturbed. The perturbations represent errors in the initial model state, and forecast errors evolve and propagate through the short-term forecast in each ensemble member. In addition to the ensemble, an unperturbed forecast is produced as the central forecast. The ensemble spread is calculated at the end of the 3-h forecast time from the difference between each ensemble member and the central forecast, and is used as a base for the estimation of the background error covariance and as the ensemble inputs to observation operators.

The Goddard Satellite Data Simulator Unit (Matsui et al. 2009) is incorporated into the forward observation operators for satellite precipitation-affected radiances. A delta-Eddington two-stream radiative transfer with slant path view (Kummerow et al. 1996) calculates the microwave brightness temperature with a given background environmental and hydrometeor state at the model resolution. The radiative transfer model is used in

TRMM operational retrieval products and its accuracies are evaluated using independent precipitation measurements (Lin and Hou 2008). To simulate the brightness temperatures as what would be observed by a spaceborne instrument, the instrument field of view (FOV) is taken into account for each sensor. A collection of simulated brightness temperatures within an observation FOV is convoluted with a Gaussian weighting to obtain one first-guess brightness temperature corresponding to the sampling location. For instance, for an observation FOV of 4 km × 7 km (85-GHz TRMM Microwave Imager) with the center at a specific latitude and longitude location, there are up to six model grid boxes within the FOV area. The simulated first-guess brightness temperatures in these model grid boxes are convolved to produce the first guess to compare with the observation. For the simulation under cloudy and precipitating condition, Mie spheres are assumed for all hydrometeors. Microphysical assumptions such as drop size distribution and ice-particle characteristics are built into the Mie calculation. Lookup tables containing extinction and scattering cross sections are precomputed to save computing time during the assimilation cycling. Dielectric properties of frozen hydrometeors are calculated based on the Maxwell–Garnett mixing theory for ice and air mixtures. Land surface emissivity is simulated as a function of polarization and surface parameters.

With the focus on cloud–precipitation data assimilation, WRF-EDAS extends its control variables to include microphysical variables (prognostic mixing ratio of rain, snow, cloud water, cloud ice, and graupel). The system uses an ensemble of nonlinear forward model simulations to link the model space and observed space, obviating the need for a tangent linear model and its adjoint for nonlinear cloud and precipitation processes. The assimilation algorithm is based on an ensemble maximum likelihood filter (Zupanski 2005; Zupanski et al. 2008), which combines ensemble-based forecast error covariance propagation and the maximum likelihood estimate to obtain an optimal analysis solution.

The maximum likelihood ensemble filter algorithm seeks the maximum of a posterior probability density function, which is achieved by an iterative minimization of a cost function:

$$J(\mathbf{x}) = \frac{1}{2}(\mathbf{x}-\mathbf{x}_b)^{\mathrm{T}}\mathbf{P}_f^{-1}(\mathbf{x}-\mathbf{x}_b) + \frac{1}{2}[\mathbf{y}-H(\mathbf{x})]^{\mathrm{T}}\mathbf{R}^{-1}[\mathbf{y}-H(\mathbf{x})], \quad (1)$$

where $\mathbf{x}$ is the best estimate of the atmospheric state represented here by the control variables including wind, temperature, moisture, and five types of hydrometeors; $\mathbf{x}_b$ represents the model forecast for the estimation problem; $\mathbf{P}_f$ is the forecast error covariance; $\mathbf{y}$ is the observation vector; H denotes the observation operators, which are nonlinear for satellite radiance observations; and $\mathbf{R}$ is the observation error covariance.

Different from traditional variational approaches with prescribed $\mathbf{P}_f$, and a tangent linear model with an adjoint for H, the maximum likelihood ensemble filter uses a control variable transformation to solve the analysis equation in ensemble space. Hessian preconditioning is defined by the following variable transformation:

$$\mathbf{x}-\mathbf{x}_b = \mathbf{P}_f^{1/2}\{\mathbf{I}+[\mathbf{z}(\mathbf{x}_b)]^{\mathrm{T}}\mathbf{Z}(\mathbf{x}_b)\}^{-1/2}\xi, \quad (2)$$

where ξ is the control variable in the ensemble space and the transformation matrix is equal to the inverse of the square root Hessian of the cost function (1). The matrix $\mathbf{Z}$ consists of column vectors that represent the difference between the perturbed and central first-guess fields in observation space. The square root analysis error covariance is obtained by the inverse of the square root Hessian via minimization. The column vectors of the square root analysis error covariance are used as perturbations for the next assimilation cycle ensemble forecasts. The algorithm belongs to the category of ensemble square root filters. If the state vector dimension is N_S, and the ensemble size is N_E, the square root forecast error covariance is an $N_S \times N_E$ matrix. For the practical reason of computing resources, the ensemble size is typically set at 32 in our experiments. To filter the noise due to a relatively small ensemble size, a localization scheme is implemented similar to the weight-interpolation method (Yang et al. 2009). The basic strategy is to partition the model domain into smaller local domains. A compactly supported covariance function of Gaspari and Cohn (1999) is employed to ensure smooth transitions between local domains. The interpolation is applied after the control variables are transformed into ensemble space, and the iterative nonlinear minimization is performed locally.

3. Tropical Storm Erin case study

a. Experiment setup

Tropical Storm Erin was formed in the Gulf of Mexico in August 2007. This tropical storm was especially difficult to predict, because after landfall it reintensified over Oklahoma on 19 August 2007, producing hurricane strength winds and heavy precipitation (Arndt et al. 2009). The case was used in a test on the prototype of the regional WRF-EDAS for evaluating the system's performance in assimilating the operational conventional

and clear-sky satellite radiances, as well as the viability of direct radiance assimilation in the system (Zupanski et al. 2011). With its compact storm structure and rapid temporal evolution, Erin provides a good case for studying the flow-dependent background error covariance estimated from ensemble forecasts, and the influence of assimilating precipitation-affected radiance observations on model-predicted precipitation.

In this experiment setting, the WRF forecasts are configured with an outer domain and an inner domain, with horizontal grid spacings of 9 and 3 km, respectively. The domain position and area are shown in Fig. 1a. The assimilation is performed every 3 h, with an ensemble size of 32. The assimilation cycling is from 1200 UTC 17 August to 1200 UTC 19 August 2007. The initial analysis covariance is constructed from 32 lagged WRF forecasts, and is used to apply perturbations to the ensemble forecasts in the first cycle. The conventional data and clear-sky radiances in selected channels of the Advanced Microwave Sounding Unit (AMSU-A, AMSU-B) and High-Resolution Infrared Radiation Sounder (HIRS) are assimilated when available in the experiment domain. Precipitation-affected radiances from the Advanced Microwave Scanning Radiometer for the Earth Observing System (AMSR-E) are assimilated at 0900 UTC 19 August 2007.

b. Forecast error covariance

Within the context of ensemble assimilation of precipitation observations, the evolution of hydrometeors from a cloud-resolving model and its associated errors are estimated using perturbed ensemble forecasts and available observations. The ensemble-estimated background error covariance is heterogeneous and flow dependent. An example is shown in Fig. 2, depicting the contrast in background error variances in precipitating and nonprecipitating regions in the case of Tropical Storm Erin. Using simulated radar reflectivity as a precipitating region mask (minimum reflectivity detection of 10 dBZ) at analysis times, the error variances of the hydrometeors and water vapor are collected at each model level and horizontally averaged in precipitating and nonprecipitating areas, respectively. It is evident that the background state uncertainty is significantly larger in the storm region; not only in hydrometeors, but also in the water vapor and temperature fields. This information will potentially allow more corrections from available observations in the area during the data assimilation procedure. Figure 3 illustrates the temporal evolution pattern of the background errors represented in the flow-dependent background error covariance. The top panels in Fig. 3 show the error standard deviations of the rainwater and water vapor at the 850-hPa model level when the storm was just moving into the inner domain. The errors in the background variables are propagated by the flow; the horizontal structure of the error standard deviations is changed and moved along the storm track as shown in the bottom panels of Fig. 3.

The off-diagonal elements in the multivariate error covariance represent the underlying relationship between errors of different variables or at different locations. Through the auto- and cross covariance, the information from an observation at one location can spread to nearby locations and to other variables as well. In the ensemble-based estimation of background error covariance, these relationships are mainly determined by the error growth associated with the dynamics and physics in forecasts. For instance, in assimilations of precipitation-affected microwave radiance over land, we rely on the scattering signals from ice or snow hydrometeors at the midlevel more than rainwater at lower levels in the atmosphere. To illustrate how error covariance responds to an isolated unit perturbation, we take a look at two variables, $\mathbf{Z}$ and $\mathbf{S}$, from an ensemble of size N_E, and the corresponding error covariance can be represented as a block matrix:

$$\mathbf{P} = \mathbf{P}^{1/2}\mathbf{P}^{\mathrm{T}/2} = \begin{pmatrix} \mathbf{Z} & \mathbf{Q} \\ \mathbf{Q}^{\mathrm{T}} & \mathbf{S} \end{pmatrix}, \tag{3}$$

where $\mathbf{Z}$ and $\mathbf{S}$ represent the error autocovariance, with diagonal elements as error variance and the off-diagonal elements as the error covariance between different locations. Here, $\mathbf{Q}$ represents the error cross covariance between the two variables, with diagonal elements for the same locations and off-diagonal ones for different locations. When an observation generates an analysis perturbation on one variable at one location, a corresponding portion of the $\mathbf{Z}$, $\mathbf{S}$, and $\mathbf{Q}$ can be plotted in model coordinates to illustrate the analysis response to the isolated unit perturbation. For example, if there is a microwave radiance observation sensitive to snow scattering at a location (34.4°N, 99.9°W), an analysis perturbation on the snow profile at the corresponding model grid at level 17 is generated. By plotting the corresponding portion of the background error cross covariance in the model grid space, Fig. 4 (top left) shows the vertical error cross covariance between this snow perturbation and the rainwater perturbation in a vertical cross section. It depicts the strong vertical correlation between forecast errors in snow content and rainwater in this storm environment. In other words, if a radiance observation senses scattering from the snow content at one location, this information will be extended to generate an analysis response in the rainwater

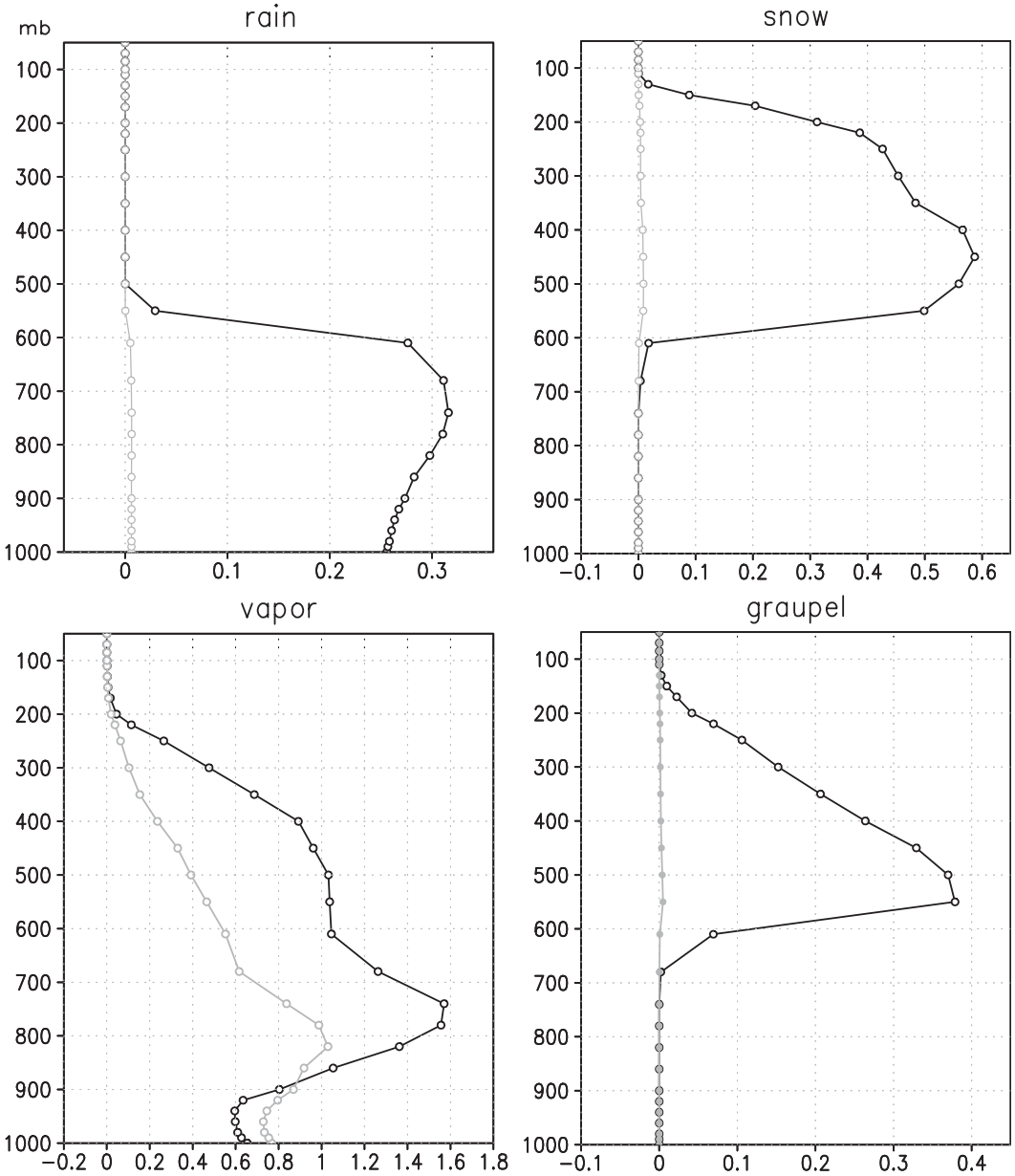

FIG. 2. Domain-averaged profiles of the background error standard deviations for precipitating (black) and nonprecipitating (gray) regions at 0300 UTC 19 Aug 2007. As labeled, the mixing ratio of rainwater, mixing ratio of snow, mixing ratio of water vapor, and graupel (all in g kg^{-1}).

in the column below and, therefore, influences the surface rainfall. Figure 4 (bottom left) shows the horizontal error cross covariance of snow and rainwater (at 850 hPa), with localized correlation length. The error cross covariance of the snow and graupel shown in Fig. 4 (top and bottom right) indicates a positive error correlation between the two microphysical variables. There are flow-dependent structures of error cross covariance between hydrometeor variables and dynamical variables, which provide a means for the observation information on hydrometeors to influence the dynamical fields as well. In this storm case, the horizontal error cross covariance between the snow perturbation and the wind indicates a vortex strengthening (not shown).

The background error covariance and control variables are crucial components of the data assimilation system. With the ensemble assimilation approach, observation information influences both the initial states and the perturbations to the ensembles. The storm displacement problem sometimes occurs in model forecasts.

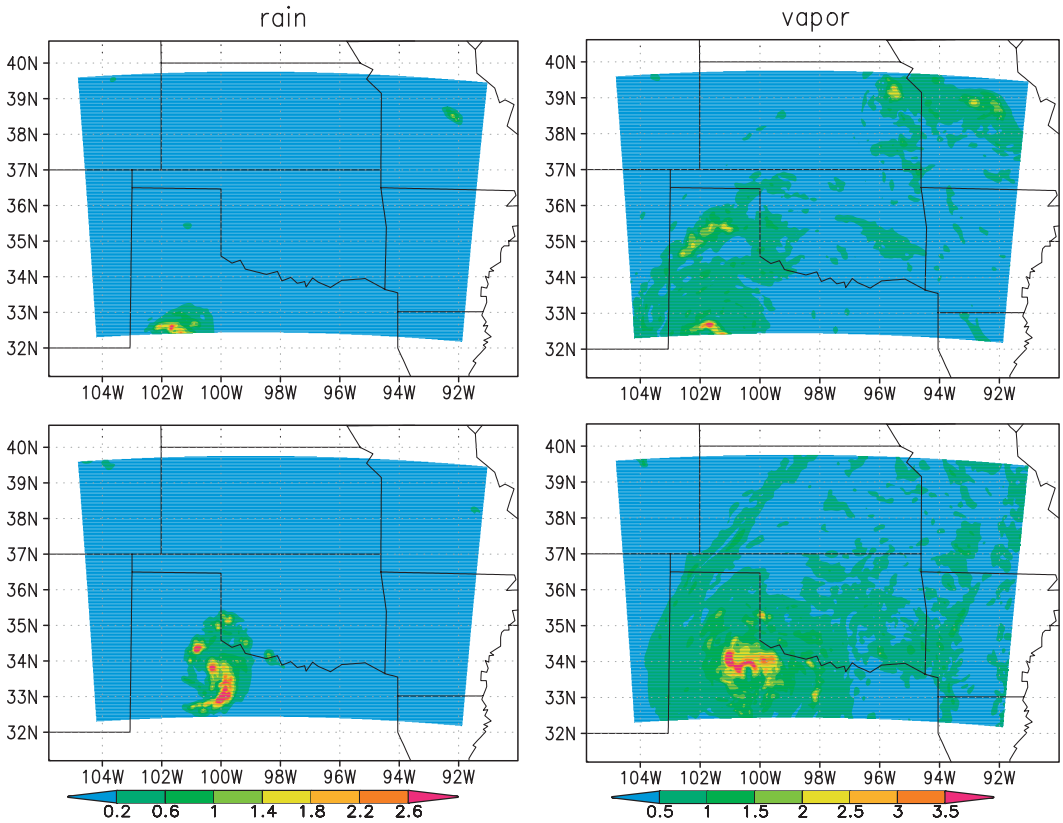

FIG. 3. The evolution of the background error standard deviation represented in the flow-dependent background error covariance at the 850-hPa model level, during Erin's reintensification period (18–19 Aug 2007). (top) The error standard deviations at 0600 UTC 18 Aug 2007 for (left) rainwater (g kg^{-1}) and (right) water vapor (g kg^{-1}). (bottom) The error standard deviations at 0300 UTC 19 Aug 2007 for (left) rainwater and (right) water vapor.

This can significantly affect the accuracy of the error covariance estimation, and the effectiveness of extracting information from observations located in the storm region. Though beyond the scope of this paper, there are ongoing research efforts to expand the ensemble spread accounting for phase errors of storms, which will be reported upon in the future.

c. *Impact of radiance observations to precipitation forecast*

From a precipitation perspective, passive microwave sensors provide measurements of the hydrometeor distribution in the atmosphere. AMSR-E is a 12-channel, six-frequency passive microwave radiometer system. It measures horizontally and vertically polarized brightness temperatures at 6.9, 10.7, 18.7, 23.8, 36.5, and 89.0 GHz. In this case study one swath of level 1b AMSR-E radiance data is available in the storm region around the peak time of the reintensification, as shown in Fig. 5a. A pair of assimilation runs is conducted using the regional WRF-EDAS for one assimilation cycle at 0900 UTC 19 August 2007. Starting from the same background, one assimilates all-sky radiance from AMSR-E at 89.0 GHz, and the other without using AMSR-E data. The observation error standard deviation for this channel is prescribed at 20 K. After the minimization the first-guess departures in 89 GHz are reduced, as shown in Fig. 5b. The error standard deviation is reduced by 31%. The impact on the surface precipitation forecast of using AMSR-E is examined by comparing the accumulated surface precipitation from two 3-h WRF forecasts issued from the analyses at 0900 UTC (with and without AMSR-E). Both forecast are in the inner domain at 3-km resolution. The ground-based stage IV surface rain observations (Lin and Mitchell 2005) are used as independent verification data, shown in Fig. 5c. The assimilation of AMSR-E in the storm region has an evident impact on the short-term precipitation forecast. The surface rain intensity distributions of two forecasts are quite different in the modest and high rain regimes, as illustrated by the histograms shown in Fig. 5d. The assimilation of the AMSR-E radiance enhanced the

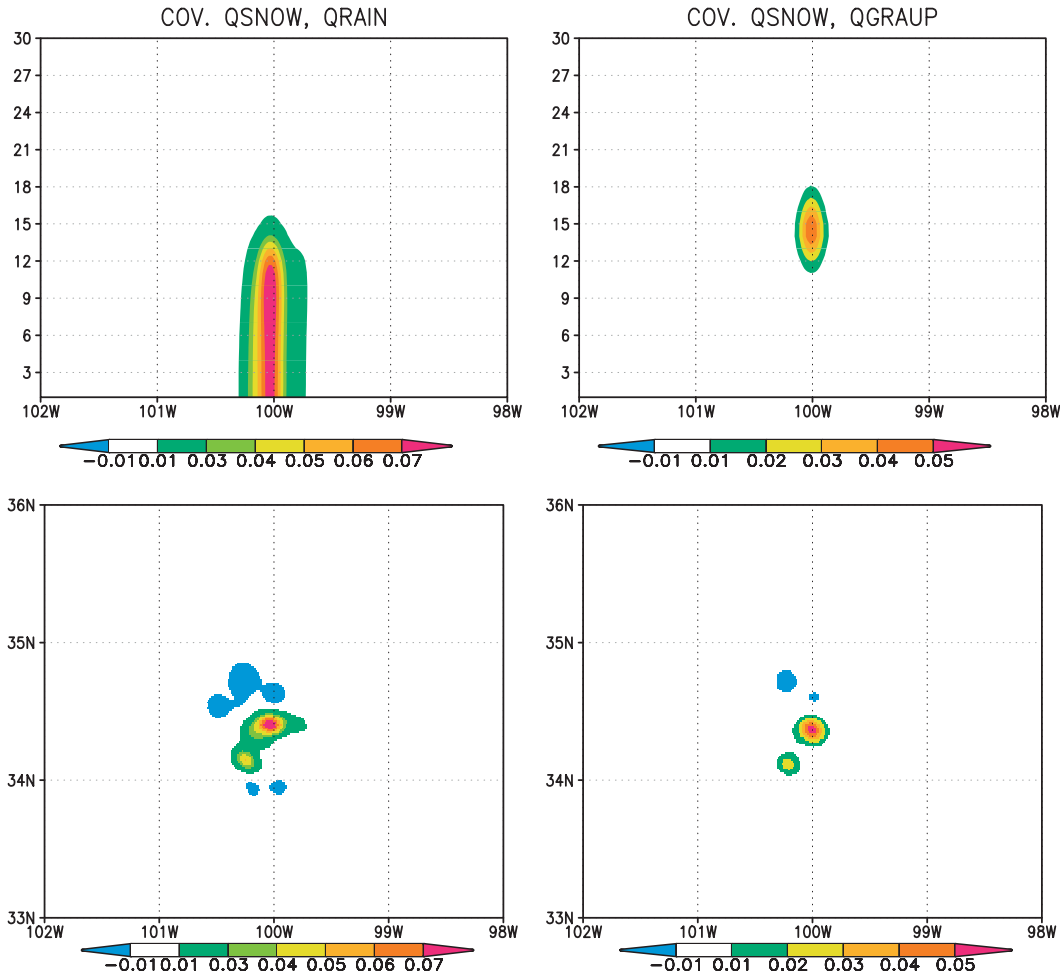

FIG. 4. Background error cross covariance, illustrated by plotting a portion of the error covariance corresponding to a single observation perturbation on the snow mixing ratio at model level 17 (600 hPa), 34.4°N, 99.9°W, validated at 0300 UTC 19 Aug 2007. (top left) Vertical error cross covariance of snow and rainwater (at 34.4°N), (bottom left) horizontal error cross covariance of snow and rainwater (at 850 hPa), (top right) vertical error cross covariance of snow and graupel (34.4°N), and (bottom right) horizontal error cross covariance of snow and graupel (at 700 hPa).

storm strength by promoting more intense precipitation, with a better level of agreement in the heavy rain bins with the distribution of verification data. There is degradation in the 40–80-mm bin, likely because analysis increments increase rain intensity only where moderate rain already exists, but fail to generate moderate surface precipitation from nonraining regimes. The precipitation forecast error standard deviation using a point-to-point comparison does not show statistically significant improvement (10.2 versus 10.3 mm for 3-h accumulation). These results illustrate the complexity encountered when transferring information in precipitation-affected radiance to subsequent surface precipitation prediction. Nevertheless, the data assimilation framework is viable for this task.

4. Experiment involving a southeastern U.S. heavy rain event

a. *Experiment design*

In September 2009 a persistent low pressure system settled over the Mississippi River valley, causing a week of heavy rain that dumped more than 10 in. across northern and central Georgia, including more than 13 in. in the Atlanta metropolitan area. It was reported that the resulting floods broke several high-water marks that dated back to 1919. We chose this case to carry out the experiment with a relatively long cycling period to collect error statistics in precipitation-affected radiance over land, and to investigate if the regional WRF-EDAS is capable of effectively using

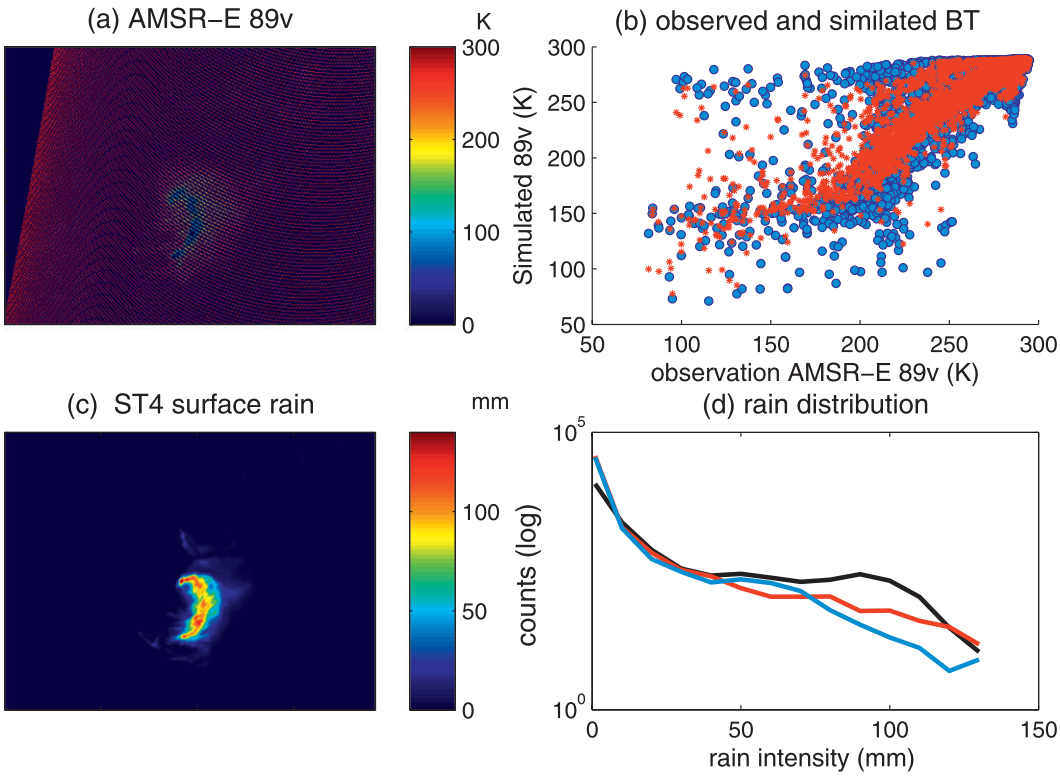

FIG. 5. Precipitation from Tropical Storm Erin. (a) Observed brightness temperature depression from the AMSR-E 89-GHz V channel at 0900 UTC 19 Aug 2007. (b) Comparison of observed 89-GHz V-channel brightness temperature with simulated brightness temperature from the first guess (blue) and the analysis (red), with a 31% reduction in the error standard deviation. (c) Stage IV surface precipitation during 0900–1200 UTC 19 Aug 2007. (d) Precipitation distribution during 0900–1200 UTC 19 Aug 2007: black, Stage IV observations; red, WRF forecast with AMSR-E assimilation; and blue, WRF forecast without AMSR-E assimilation.

precipitation-affected radiance data to reduce errors in WRF precipitation.

The WRF forecast is configured with two domains in the southeastern United States (Fig. 1), with 9- and 3-km grid spacing, respectively. The cycling period starts at 1200 UTC 12 September 2009, and runs for 80 cycles total with a 3-h assimilation interval. The ensemble size is 32. In the first cycle, the initial perturbations to the ensemble forecasts are generated from a covariance of 32 lagged forecasts, and the global analysis is interpolated into the resolution of the outer domain as the initial conditions. It takes about four cycles to spin up the ensemble system with dynamical state updates in the background error covariance. We use the entire cycling period for monitoring the overall system performance, and we use the heavy rain event in Georgia from 15 to 22 September 2009 for statistics of radiance innovations and accumulated precipitation.

Parallel to the WRF-EDAS assimilation cycling, a WRF gridpoint statistical interpolation 3DVAR run is carried out as a reference control experiment (WRF-GSI-CNTR). The differences in this control experiment and the ensemble assimilation system are summarized in Table 1. The contrast between the reference control and the ensemble assimilation emphasizes the new features of the regional WRF-EDAS, so that comparisons of the results in analyses and precipitation forecasts provide an evaluation of the performance of the regional WRF-EDAS and its capability to use precipitation-affected radiance data.

In addition to the two assimilation runs mentioned above, a data denial experiment (WRF-EADS-CNTR) is also performed to focus on the precipitation-affected radiance data impact upon the WRF ensemble assimilation system. It is configured in the same way as the WRF-EDAS run, but without using observations of precipitation-affected radiances.

All experiments use a common set of conventional data and clear-sky radiances from selected AMSU-A and Atmospheric Infrared Sounder (AIRS) channels. The quality control and bias correction on these data are applied using the schemes from the operational GSI system. In addition, the WRF-EDAS run uses precipitation-affected radiances from AMSR-E and TRMM Microwave

TABLE 1. Experiment system comparison: WRF-EDAS and WRF-GSI for the case of the southeastern U.S. heavy rain event.

Experiment system	Regional WRF-EDAS	Regional WRF-GSI
Control variable	U, V, P, Q, T, Rain, snow, graupel, cloud water, cloud ice	U, V, P, Q, T
Background error covariance	Flow dependent	Prescribed
Observations	Conventional data Clear-sky AMSU-A AIRS Precipitation-affected AMSR-E, TMI	Conventional data Clear-sky AMSU-A, AIRS
Radiance simulator	Clear-sky radiance transfer model for AMSU-A, AIRS All-sky radiance transfer model for AMSR-E, TMI	Clear-sky radiance transfer model for AMSU-A, AIRS

Imager (TMI) level 1b data. TMI provides channels from 10 to 85 GHz, with vertical and horizontal polarization (V or H): 10V/H, 19V/H, 22V, 37V/H, and 85V/H, with FOV sizes of 60 km × 36 km, 30 km × 18 km, 27 km × 16 km, 16 km × 10 km, and 7 km × 4 km, respectively.

b. Observational errors and data selection

In direct radiance assimilation, the departure of a model-simulated radiance from observations is expressed as the radiance innovation $[\mathbf{y} - H(\mathbf{x})]$, where $\mathbf{y}$ is the brightness temperature observed by the microwave instrument and $H(\mathbf{x})$ is the simulated radiance through a nonlinear observation operator, consisting of a spatiotemporal matching and a radiative transfer model. All of the observations within 90 min of the current analysis time are included. Each observed radiance pixel centered at a geophysical location is collocated with a model grid point using a nearest-point scheme. Then, the model grid point is used as the center point of the FOV of the beam convolution for the simulated radiance. Finally, the radiance innovation is calculated at each collocated grid point.

The choice of the channels is based on the surface type. Over land, the scattering signature from the frozen precipitation aloft is the dominant information source for inferring precipitation reaching the surface. In this experiment the high-frequency 89-GHz AMSR-E and 85-GHz TMI channels are selected for their sensitivity in registering scattering signals. The rest of the channels are not assimilated due to the difficulty in distinguishing emission signatures of liquid water content in the atmosphere from the highly variable land surface.

The data selection for precipitation-sensitive radiance considers three scenarios at each observed location: 1) the observation detects precipitation, but the first guess indicates no precipitation; 2) the first guess shows precipitation, but the observation is not able to detect precipitation; and 3) both the observation and the first guess agree on the precipitating conditions. The observations at locations fitting these scenarios are selected into the assimilation procedure. For our targeted application of assimilating precipitation-affected radiance over land, a screening approach following Wilheit et al. (2003) is adapted from precipitation retrievals over land. At each observation location, a scattering index for land (SIL) is calculated as a measure of depression due to scattering by precipitation:

$$\mathrm{SIL} = 451.9 - 0.44\mathrm{Tb}_{19\mathrm{V}} - 1.775\mathrm{Tb}_{21\mathrm{V}} + 0.005\,75\mathrm{Tb}_{21\mathrm{V}}^2 - \mathrm{Tb}_{85\mathrm{V}}. \quad (4)$$

A location is identified as in the precipitating region if the SIL value is greater than 10 K. At each location two SIL values are calculated: one from the observed radiance and one from the simulated radiance. The values of the two SIL results determine to which scenario, as described above, the current location will belong. An example of using SIL to identify precipitating region is given in Fig. 6. The top panel shows the ground observations of surface rain from stage IV data. The middle panel in Fig. 6 shows the brightness temperatures from the TMI 85-GHz V channel, with significant brightness temperature depression. The SILvalues based on signals from three TMI channels are plotted in the bottom panel of Fig. 6, where the area of SIL values greater than 10 K shows high correlation with the precipitating region as indicated in the ground observations.

With the data selection described above, radiance innovations are sampled from observations and simulations to generate observation error statistics. Figure 7 shows the histograms of radiance innovation of the TMI 85-GHz V channel, sampled from the sustained precipitation event (15–22 September 2009). Unlike clear-sky radiance observations, the precipitation-affected radiance innovation distributions have different bias characteristics that depend on the precipitation condition at sampling locations. For instance, the top panel in Fig. 7 shows a 6-K bias sampled over where both the first guess and the observation agree there is precipitation. The middle panel in Fig. 7 shows a collection of samples

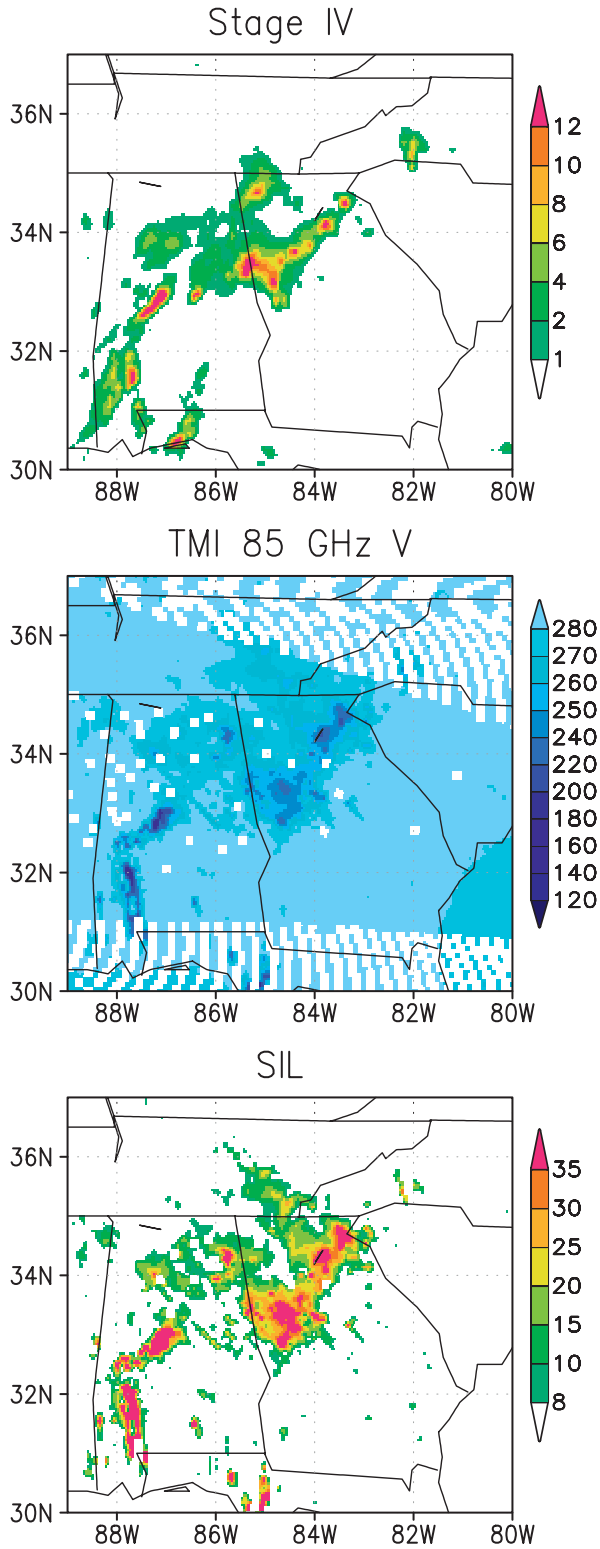

FIG. 6. Observed precipitation in the southeastern United States at 1800 UTC 19 Sep 2009: (top) surface rainfall from stage IV data (mm h^{-1}), (middle) TMI 85-GHz V radiance observations (K), and (bottom) SIL results based on signals from TMI 19-GHz V, 21-GHz V, and 85-GHz V channels (K).

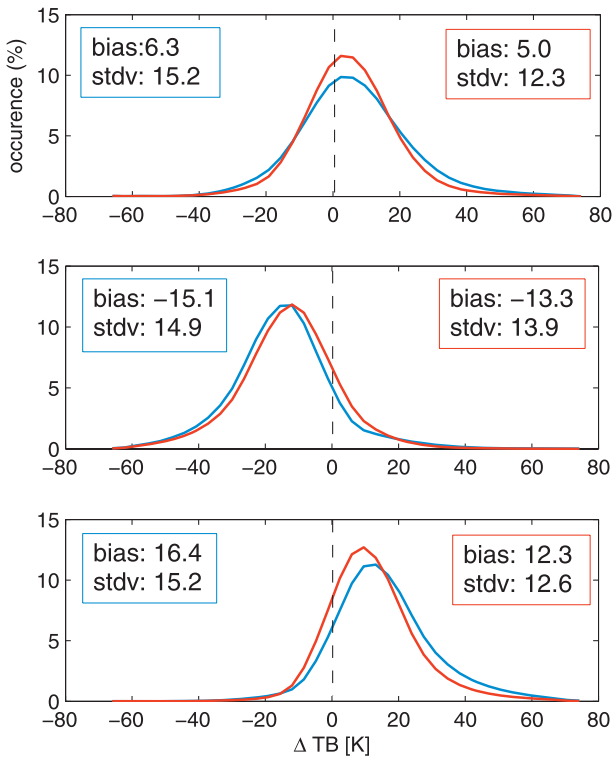

FIG. 7. Histograms of radiance innovation from the TMI 85-GHz V channel, sampled from the WRF-EDAS experiment of the southeastern U.S. heavy rain event (15–22 Sep 2009): blue, first-guess departure; red, analysis departure. Samples taken where (top) both the first guess and the observation indicate precipitation, (middle) the first guess indicates no precipitation but the observation detects rain, and (bottom) the first guess indicates precipitation but the observation indicates no rain.

where the first guess indicates no precipitation, but the observations detect rain; therefore, the distribution exhibits a negative mean (observations show a brightness temperature depression, while first guesses have typical clear-sky brightness temperatures). The bottom panel in Fig. 7 shows an opposite bias sampled over where the first guess indicates precipitation while the observations indicate no rain. This phenomenon poses a challenge for developing an effective bias correction method for precipitation-affected radiance. The predictors chosen for clear-sky conditions are no longer suitable, and new predictors need to reflect the precipitation conditions represented both in the first guess and the observations. In the current implementation, no online bias correction is applied to the radiance observations under precipitation conditions. The observation error standard deviations are defined with consideration taken of different scenarios, particularly over where the observations and model simulations disagree on precipitation conditions. In this experiment the radiance observation error standard deviations for 85-GHz TMI data are

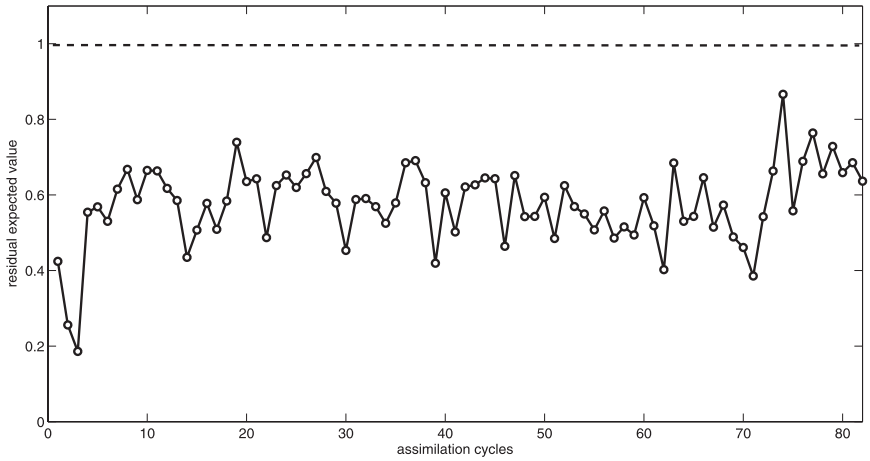

FIG. 8. The time series of the a posteriori residual χ^2 expectation calculated from all observations assimilated at each analysis time during 80 assimilation cycles (1200 UTC 12 Sep–1200 UTC 22 Sep 2009).

prescribed at 15 K for scenario 1 and 20 K for scenarios 2 and 3. The observation errors are assumed to be spatially uncorrelated. A similar procedure is performed for AMSR-E data, with error standard deviations of 18 K for scenario 1 and 20 K for scenarios 2 and 3. The current quality control process rejects an observation where the innovation is larger than 3 times the observation error standard deviation in any of the scenarios. A new predictor using observation-based and simulation-based SIL is being developed for bias correction and quality control, with an approach similar to the symmetric cloud amount method proposed in Geer and Bauer (2011).

It should be noted that the microwave observations at high frequency have low sensitivity to shallow warm precipitation. There are cases in which the observations do not detect precipitation where warm rain is present at lower levels. This can cause a positive bias in radiance innovations in light, warm rain regions. In the current system this issue is not yet addressed, and there are plans to develop a bias correction scheme to overcome this problem using information from low-frequency signals and observation-based land surface emissivity estimation.

c. *Analysis performance*

The WRF-EDAS assimilates the observations mentioned above and a minimization procedure is carried out at each analysis time in ensemble space. The result is projected in observation space as minimized departures between the observed and estimated radiances. As shown in Fig. 7 comparing the first-guess departure (blue) and the analysis departure (red), the discrepancies between the observed and model-simulated radiances in precipitation regions are reduced, with the analysis error variance smaller than that of the first guess. The radiance departures for the first guess and analysis are sampled at observation locations. This demonstrates the capability of the ensemble assimilation system in making corrections to hydrometeors and other precipitation-related state variables via minimization of the discrepancy between model-simulated and instrument-observed radiances in precipitating regions.

The error covariance of the least squares estimates can be expressed in terms of the error covariance of the data. We define $\mathbf{r}$ as normalized innovations after the analysis solution is obtained and weighting the data as described in the cost function (1):

$$\mathbf{r} = (\mathbf{R} + \mathbf{HPH}^{\mathrm{T}})^{-1/2}[\mathbf{y} - H(\mathbf{x}_a)]. \tag{5}$$

The statistical properties of the a posteriori residual $\mathbf{r}^{\mathrm{T}}\mathbf{r}$ are a function of the observation and background errors. The χ^2 property (Tarantola 1987, section 4.3.6) states that if observation and background errors are uncorrelated and with a correct estimation of their covariance, the a posteriori residual has the χ^2 distribution with m degrees of freedom, where m is the total number of observations. Therefore, the expected value of the residual should equal m; in other words, the following expected quantity should be close to unity:

$$E\left[\frac{\mathbf{r}^{\mathrm{T}}\mathbf{r}}{m}\right] = 1. \tag{6}$$

A deviation of the residual from the expected value can be used to evaluate the validity of the ensemble-estimated background error covariance and the prescribed observation error covariance. Figure 8 presents the time series of residual expectations as defined in (6) calculated

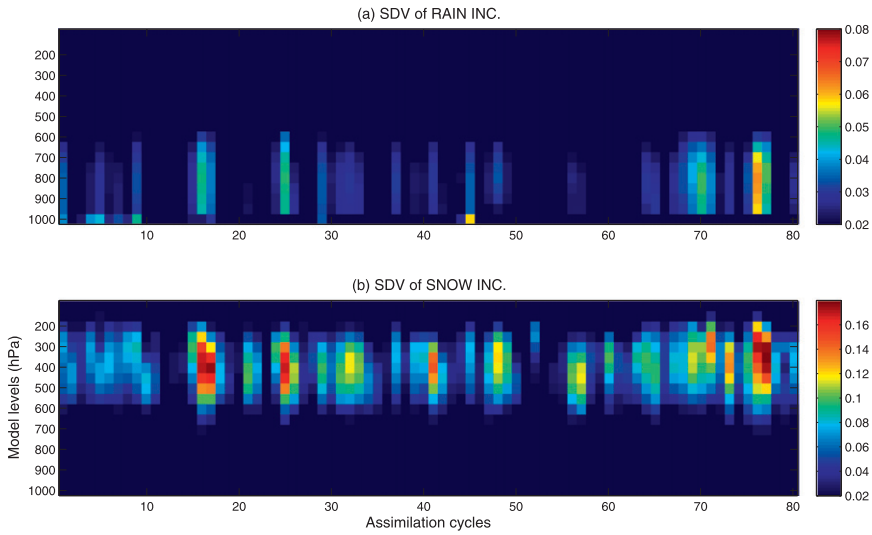

FIG. 9. Time–vertical profiles of standard deviation of hydrometeor analysis increments horizontally averaged during the assimilation cycling period of the WRF-EDAS experiment (g kg^{-1}): (a) rainwater and (b) snow water mixing ratio increments.

from all observations used at each analysis time. It is observed that during the spinup of the assimilation cycling the expected value of the residual divided by m is much less than unity, indicating a significant overestimate of background errors during the initial period. Then, the quantity stabilizes around a mean value of 0.5 through the rest of the assimilation cycling period, implying that the ensemble-estimated background error covariance becomes more realistic without signs of filter divergence. In the meantime, the prescribed observation error covariance may need to be reexamined and tuned to better represent the underlying errors reflected in the residual statistics.

The assimilation of precipitation-affected radiance produces analysis increments on all control variables. The most directly related examples are hydrometeors. In Fig. 9 the standard deviations of the hydrometeor analysis increments in the domain are illustrated as time-vertical profiles, calculated as horizontally averaged in the domain and recorded during the assimilation cycling period. The vertical structure of the increments is largely determined by the cloud-resolving model physics and the sensitivities of simulated radiance to the changes of hydrometeor distributions in the atmosphere, and the data information is spread by the background error auto- and cross covariances between variables. In assimilation of microwave radiance of high frequencies over land, the sensitivity concentrates on frozen hydrometeors such as snow mixing ratio (the standard deviation shown in the bottom panel of Fig. 9). Nevertheless, the observation information gets propagated onto rainwater increments (the standard deviation shown in the top panel of Fig. 9). Since the precipitation-affected microwave radiances mainly respond to the total column of hydrometeors in the atmosphere, we show the distributions of hydrometeor analysis increments in the form of total water path in Fig. 10 in rainwater, snow, cloud water, and water vapor. There are no significant biases in the distributions, and the standard deviations are comparable to the analysis error statistics.

d. *Impact to WRF forecasts*

To examine the impact of ensemble assimilation of precipitation-affected radiance on the short-term forecasts, in particular the surface precipitation, quantitative precipitation forecasts are carried out and initialized by the analyses from the WRF-EDAS assimilation, and WRF-GSI-CNTR and WRF-EDAS-CNTR, as described in the experiment configuration. Stage IV surface rain observations are used as the independent verification data. The forecasts are initialized by the analyses at 3-h intervals, and surface precipitation accumulations are summed for the period 15–22 September 2009. Figure 11 shows the accumulated surface rain during the flooding period, with stage IV observations, WRF-EDAS initialized results, WRF-GSI-CNTR initialized results, and WRF-EDAS-CNTR initialized results. All data in the comparisons are at 3-km resolution, with verification data remapped from 4- to 3-km grids. WRF-EDAS assimilation results show a better level of agreement with the observed verification in the reported flooding region of northern Georgia. WRF-EDAS results have a smaller bias of 24 mm comparing with 41 mm for WRF-GSI-CNTR, and a bias that is slightly bigger

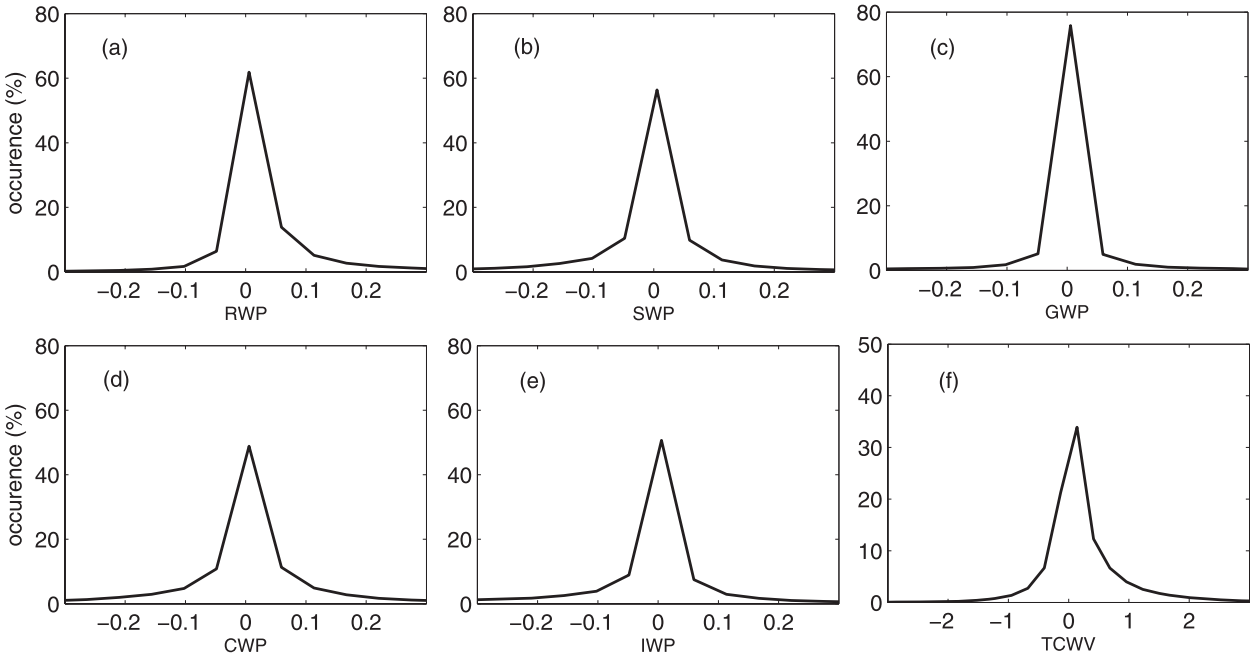

FIG. 10. Histograms of hydrometeor analysis increments (integrated vertically as the total-column water path, g m^{-2}), sampled from the WRF-EDAS experiment during 15–22 Sep 2009, for the (a) rainwater path, (b) snow water path, (c) graupel water path, (d) cloud water path, (e) cloud ice water path, and (f) total-column water vapor.

than 21 mm for WRF-EDAS-CNTR, as well as a smaller error standard deviation of 48 mm versus 55 and 53 mm in the WRF-GSI-CNTR and WRF-EDAS-CNTR results, respectively. These results demonstrate that the ensemble assimilation of satellite precipitation observations brings more information about precipitation processes to the analysis, which in turn improves the accuracy of the quantitative precipitation forecasts. The comparison between WRF-EDAS and WRF-EDAS-CNTR further illustrates the data impact within the ensemble assimilation framework, with enhanced rainfall in Georgia and reduced precipitation in Tennessee. There is a negligible impact in Alabama, where the radiance assimilation fails to promote substantial rainfall comparing to the verification data. The first guess in this region is dry in WRF-EDAS, and the magnitude of the ensemble perturbations to the hydrometeor control variables is relatively small. These conditions limit the analysis solution without significant corrections to the precipitation process in the region being necessary. It is also observed that the scattering signals in microwave observations in this region are weak compared with those in Georgia, indicating a warm rain system observed by ground-based data, but not well observed by microwave high-frequency channels.

The precipitation assimilation impact on high-resolution precipitation forecasts at different spatial scales and different rain intensities is also examined using a neighborhood verification method fractions skill score (FSS; Roberts and Lean 2008). FSS evaluates high-resolution precipitation forecasts by comparing the fractional coverage of events in windows surrounding the observed and forecast rain events:

$$\mathrm{FSS} = 1 - \frac{\frac{1}{N}\sum_{N}(S_{\mathrm{fcst}} - S_{\mathrm{obs}})^2}{\frac{1}{N}\left[\sum_{N}(S_{\mathrm{fcst}})^2 - \sum_{N}(S_{\mathrm{obs}})^2\right]}, \tag{7}$$

where S_{fcst} and S_{obs} are the fractional coverages of the forecast and observed grid box rain events, respectively, in each of the N windows in the domain. The spatial size of the window can be varied from one grid box per window (point-to-point evaluation), to all grid boxes in one window (full-domain comparison). This verification approach considers the characteristics of high-resolution quantitative precipitation forecasts by assessing the degree of closeness in terms of the scale-dependent and intensity-dependent performance (Ebert 2009). Table 2 displays the array of FSS values for a 24-h accumulated surface rain forecast in the domain with 3-km grid spacing, from 0000 UTC 19 September to 0000 UTC 20 September 2009. In Table 2 (top) the forecast is initialized by WRF-EDAS analysis assimilated TMI and AMSR-E radiances, while in Table 2 (bottom) the forecast is initialized by WRF-GSI-CNTR analysis without assimilating precipitation-affected radiances. The FSS

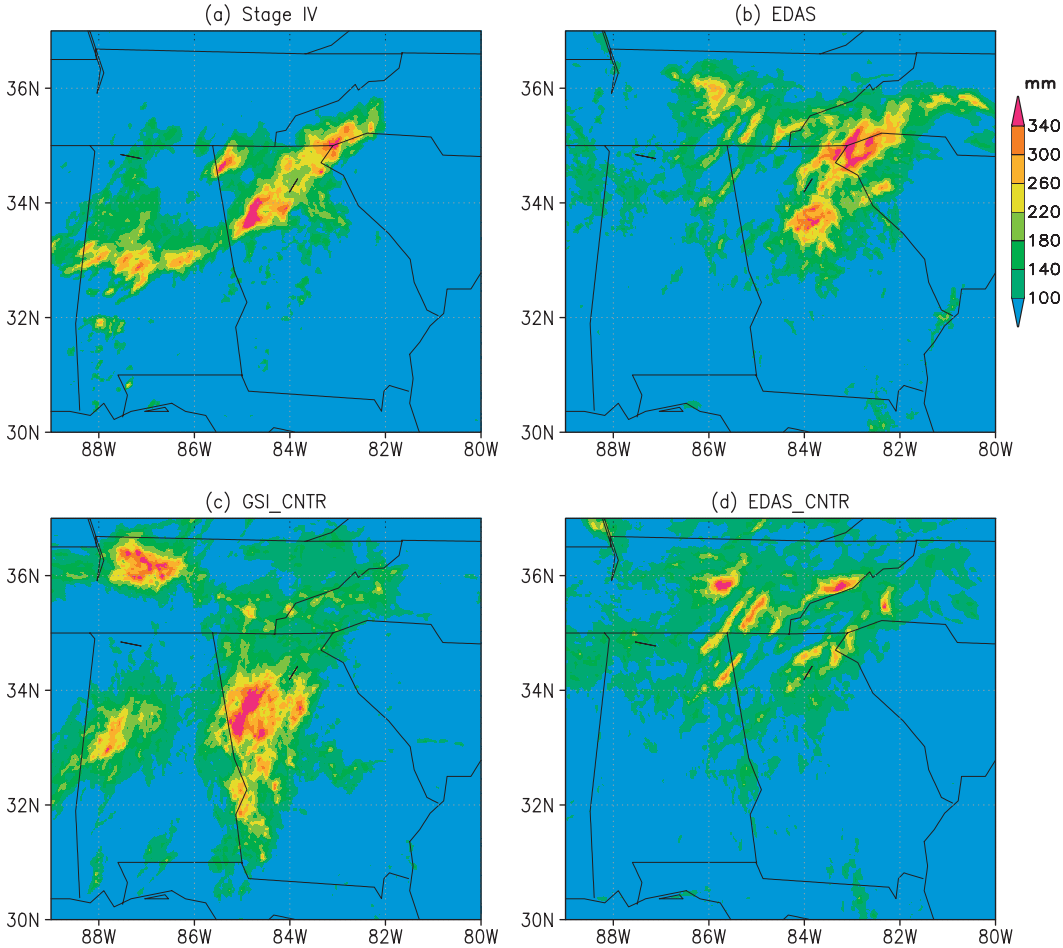

FIG. 11. Surface rainfall accumulated during 15–22 Sep 2009 (mm), with 3-km spatial resolution: (a) stage IV verification data, (b) forecasts initialized every 3 h by the analysis of WRF-EDAS assimilating TMI and AMSR-E, (c) forecasts initialized by the analysis of WRF-GSI without assimilating TMI and AMSR-E radiances, and (d) forecasts initialized by the analysis of WRF-EDAS without assimilating TMI and AMSR-E.

scores are calculated against the verification data of stage IV surface rain observations with the original 4-km resolution interpolated to WRF 3-km grid spacing in the domain. The verifications are segregated into different spatial scales from 3 to 195 km that determine the sizes of the local neighborhoods, and different rain intensities from 0.1 to 50 mm day^{-1}. It is observed that the level of precipitation forecast skill improves with increasing spatial scale and decreasing rain intensity. A comparison of the scores from two forecasts shows that the assimilation of TMI and AMSR-E observations has a positive impact on the forecasts in the category of moderate to high rainfall at all spatial scales. Overall, the skill of the precipitation forecasts at high resolution needs further improvement to be considered "useful" for operational forecasts, which is often evaluated according to the target criterion that the FSS score is higher than 0.5 plus half of the fraction of the observed grid-box events in the full domain, as is indicated by the boldfaced entries in Table 2.

The model physics and dynamics interact during the forecasts. The assimilation of precipitation observations also has an impact on the dynamical fields. The RMS errors of the 3-h forecasts are verified against the available conventional in situ data during the assimilation cycling period. As shown in Fig. 12, the forecast errors of WRF-EDAS are mostly smaller or comparable to those of WRF-GSI-CNTR for wind, temperature, and moisture, an indication of the benefits of using precipitation information from radiances and ensemble-based forecast error covariance.

5. Conclusions

An ensemble data assimilation system, the NASA regional WRF-EDAS, has been developed to assimilate

TABLE 2. FSS for 24-h accumulated surface rain forecast in the inner domain at 3-km resolution, from 0000 UTC 19 Sep to 0000 UTC 20 Sep 2009. (top) Forecast initialized from WRF-EDAS analysis with TMI and AMSR-E radiances assimilated. (bottom) Forecast initialized from WRF-GSI analysis without assimilating TMI and AMSR-E radiances. The scores are calculated against the stage IV surface rain observation data at 4-km resolution, interpolated to model 3-km grid. The boldface entries indicate the scores that meet the target criterion for operational forecasts.

	Rain threshold (mm day^{-1})							
Spatial scale (km)	0.1	0.5	1.0	2.0	5.0	10.0	20.0	50.0
195	**0.94**	**0.92**	**0.91**	**0.88**	**0.82**	**0.75**	**0.72**	0.42
99	**0.91**	**0.88**	**0.85**	**0.81**	**0.76**	**0.69**	**0.66**	0.32
51	**0.90**	**0.85**	**0.81**	**0.76**	**0.68**	**0.61**	**0.58**	0.32
27	**0.88**	**0.83**	**0.78**	**0.73**	**0.64**	**0.56**	**0.53**	0.27
15	**0.87**	**0.81**	**0.76**	**0.70**	**0.60**	**0.53**	0.49	0.25
9	**0.86**	**0.80**	**0.75**	**0.68**	**0.58**	0.50	0.46	0.23
3	**0.83**	**0.76**	**0.70**	**0.63**	**0.52**	0.44	0.40	0.20
	Rain threshold (mm day^{-1})							
Spatial scale (km)	0.1	0.5	1.0	2.0	5.0	10.0	20.0	50.0
195	**0.94**	**0.92**	**0.90**	**0.84**	**0.70**	**0.57**	0.49	0.48
99	**0.91**	**0.89**	**0.85**	**0.78**	**0.63**	0.49	0.36	0.22
51	**0.90**	**0.87**	**0.83**	**0.76**	**0.60**	0.43	0.29	0.12
27	**0.88**	**0.85**	**0.80**	**0.73**	**0.56**	0.40	0.24	0.10
15	**0.87**	**0.83**	**0.78**	**0.71**	**0.53**	0.37	0.21	0.07
9	**0.86**	**0.82**	**0.77**	**0.69**	**0.52**	0.35	0.19	0.06
3	**0.84**	**0.79**	**0.74**	**0.65**	0.47	0.31	0.16	0.04

spaceborne microwave radiances affected by clouds and precipitation. With an emphasis on hydrological applications such as the dynamical downscaling of satellite observations of precipitation processes, the technical implementation of the system pays special attention to the issues unique to direct radiance assimilation with cloud and precipitation information: 1) the choice of including hydrometeors among the control variables for their direct linkages to cloud and precipitation physics and the sensitivity of radiance under precipitation conditions, 2) the choice of cloud-resolving resolution in ensemble model forecasts for simulating radiance with spatial representations comparable to those of the observations, 3) the use of ensemble forecasts for estimating the flow-dependent background error covariance, and 4) the use of ensemble perturbation-based covariance to project information between the observation space and the model space, bypassing explicit linearization and the adjoint of nonlinear cloud physics and the radiative transfer.

This paper has described how the flow-dependent background error covariance is estimated and updated in the assimilation procedure, and how the information in a radiance observation is propagated via background error auto- and cross covariance to impact the entire analysis state. This paper also presents an error statistical description in observational radiance space, and the data quality control procedure specified for using radiance observations over land. The system performance is evaluated via experiments assimilating AMSR-E and TRMM TMI radiance observations during a tropical storm (Erin) reintensification over land during August 2007 and a heavy rain event in the southeastern United States during September 2009.

Compared with the WRF-GSI scheme, a 3DVAR clear-sky radiance data assimilation system with a static background error covariance, WRF-EDAS more effectively utilizes precipitation-affected radiance data to correct forecast errors in the region with clouds and precipitation. Due to the ambiguity in signals of low-frequency channels caused by variations in the land surface emissivity, only the high-frequency channels of 85 GHz (TMI) and 89 GHz (AMSR-E) are assimilated over land. Several low-frequency channels are used in the calculation of the scattering index that serves as a criterion for identifying the presence of precipitation for data selection and observation error specification. The case study of Tropical Storm Erin (August 2007) illustrates the flow dependency of the background error covariance in WRF-EDAS. The background error variance evolves along with the storm track and intensity. The error cross covariance among the control variables, particularly between frozen and liquid hydrometeors, plays an important role in propagating information from high-frequency channel radiance observations, which influence the precipitation analysis. A comparison of observed and simulated radiances in conjunction with ground-based rain observations indicates that the hydrometeor distributions modified by analysis increments from radiance assimilation are improved in representing the precipitation process in the atmosphere. Using independent ground-based measurements of surface rainfall as verification, the southeastern U.S. heavy rain event (September 2009) experiment demonstrates that precipitation-sensitive radiance assimilation in WRF-EDAS improves the spatial distribution and intensity in the accumulated surface rainfall and achieves better short-term quantitative precipitation forecasts, as evaluated by the fraction skill score. In addition, the precipitation data's impact within the WRF ensemble data assimilation framework is examined by use of a data denial experiment, and the results provide evidence that information in precipitation-affected radiance observations provides a positive impact on the WRF precipitation in regions with adequate magnitudes of background error covariance.

The experience of the WRF-EDAS development and assimilation experiments has not only highlighted the potential of the current system in utilizing precipitation-affected radiances, but also revealed issues requiring further development and investigation. First, because

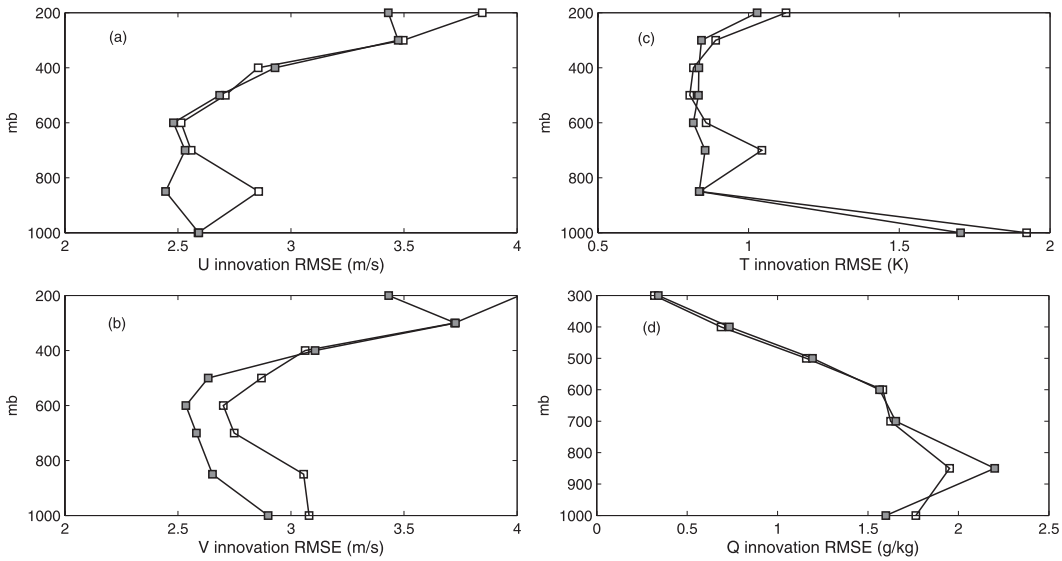

FIG. 12. Vertical profiles of the first-guess departures from WRF-EDAS (with filled square) and WRF-GSI (with open square). RMS errors for the (a) u-wind component, (b) v-wind component, (c) temperature, and (d) specific humidity. The errors are calculated with respect to the NCEP conventional observations available during data assimilation cycling from 1200 UTC 12 Sep to 1200 UTC 22 Sep 2009.

the ensemble WRF forecasts play a crucial role not only in providing the first guess, but also in estimating the flow-dependent background error covariance. Certain types of model errors such as systematic precipitation system displacement, combined with insufficient ensemble size, will have a profound impact on the effectiveness and quality of the precipitation radiance assimilation. Further research and development aimed at addressing these issues are under way, for instance, expanding the forecast ensemble and developing a hybrid approach to account for displacement errors where ensemble forecasts fail to predict clouds and precipitation. Second, the high-frequency channel radiance tends to be ''blind'' to warm rain processes over land, and this lack of sensitivity can lead to a misinterpretation of radiance innovations by the assimilation system, which may erroneously reduce or remove warm precipitation presented in the first guess. There is a development plan for including more microwave sounder observations and radar observations for better detecting warm rain over land. The issue of an effective cycling length is unique to a data assimilation system with limited-area model forecasts. More research and experiments need to be done to gain an insight into the optimal cycling length for effectively propagating the background error covariance, for retaining microphysical features, and at the same time for correctly maintaining the large-scale forcing in domain interiors over a total cycling period. Last, but not the least, the current localization scheme for ensemble-based background error covariance estimation has fixed localization parameters for all variables and observation types. Efforts will be made to experiment on the adaptive localization scheme according to the observation physical characteristics and spatial scales.

Ensemble data assimilation in limited areas at high resolution has made significant progress in applications using conventional direct observations on atmospheric state and indirect observations in forms of ground-based radar data. However, for applications using satellite observations, particularly under cloudy and precipitating conditions, the research is still in its infancy (Meng and Zhang 2011). The development of WRF-EDAS for the application of dynamic downscaling of satellite precipitation observations provides a starting point to explore this potential and address challenges. To produce a coherent and accurate precipitation estimate by combining information from available data sources, the ensemble data assimilation approach presented here differs from purely observation-based estimation and statistical downscaling techniques, mainly in employing a priori information on the background state from a numerical forecast model to achieve a maximum likelihood solution. The dynamics and physics described in a state-of-the-art numerical forecast model represent a progressive understanding of the nature and the mechanism of atmospheric states and processes, with knowledge accumulated and insight gained through the collective efforts of scientific research, experiments, and observations. It is recognized that the model forecast skill of

precipitation forecasting still lags behind that of other weather and climate fields, largely due to the level of complexity and the unpredictability of the cloud and precipitation phenomena. Nevertheless, there are advantages in using forecast models, including providing dynamical and physical consistency and complete spatial–temporal coverage at the desired resolution. While future work is needed to improve the performance of WRF-EDAS, this system's development provides a useful platform for advancing cloud and precipitation assimilation techniques that utilize satellite observations of precipitation processes.

Acknowledgments. This research was supported by the Global Precipitation Measurement (GPM) Flight Project at NASA Goddard Space Flight Center, and NASA Precipitation Measurement Mission (PMM) Science Program under Grant NNX07AD75G to Colorado State University. Computations were carried out at NASA Advanced Supercomputing (NAS). We thank the anonymous reviewers for their improvements to the paper.

REFERENCES

Arndt, D. S., J. B. Basara, R. A. McPherson, B. G. Illston, G. D. McManus, and D. B. Demko, 2009: Observations of the overland reintensification of Tropical Storm Erin (2007). *Bull. Amer. Meteor. Soc.,* **90,** 1079–1093.

Bauer, P., P. Lopez, A. Benedetti, D. Salmond, and E. Moreau, 2006a: Implementation of 1D+4D-Var assimilation of precipitation-affected microwave radiances at ECMWF. I: 1D-Var. *Quart. J. Roy. Meteor. Soc.,* **132,** 2277–2306.

——, ——, ——, ——, S. Saarinen, and M. Bonazzola, 2006b: Implementation of 1D+4D-Var assimilation of precipitation-affected microwave radiances in precipitation at ECMWF. II: 4D-Var. *Quart. J. Roy. Meteor. Soc.,* **132,** 2307–2332.

——, A. Geer, P. Lopez, and D. Salmond, 2010: Direct 4D-Var assimilation of all-sky radiances. Part I: Implementation. *Quart. J. Roy. Meteor. Soc.,* **136,** 1868–1885.

Buehner, M., P. L. Houtekamer, C. Charette, H. L. Mitchell, and B. He, 2010a: Intercomparison of variational data assimilation and the ensemble Kalman filter for global deterministic NWP. Part I: Description and single-observation experiments. *Mon. Wea. Rev.,* **138,** 1550–1566.

——, ——, ——, ——, and B. He, 2010b: Intercomparison of variational data assimilation and the ensemble Kalman filter for global deterministic NWP. Part II: One-month experiments with real observations. *Mon. Wea. Rev.,* **138,** 1567–1586.

Dowell, D. C., L. J. Wicker, and C. Snyder, 2011: Ensemble Kalman filter assimilation of radar observations of the 8 May 2003 Oklahoma City supercell: Influences of reflectivity observations on storm-scale analyses. *Mon. Wea. Rev.,* **139,** 272–294.

Ebert, E., 2009: Neighborhood verification: A strategy for rewarding close forecasts. *Wea. Forecasting,* **24,** 1498–1510.

Errico, R., J.-F. Mahfouf, and P. Bauer, 2007: Issues regarding the assimilation of cloud and precipitation data. *J. Atmos. Sci.,* **64,** 3785–3798.

Gaspari, G., and S. E. Cohn, 1999: Construction of correlation functions in two and three dimensions. *Quart. J. Roy. Meteor. Soc.,* **125,** 723–757.

Geer, A. J., and P. Bauer, 2011: Observation errors in all-sky data assimilation. *Quart. J. Roy. Meteor. Soc.,* **137,** 2024–2037.

——, ——, and P. Lopez, 2010: Direct 4D-Var assimilation of all-sky radiances. Part II: Assessment. *Quart. J. Roy. Meteor. Soc.,* **136,** 1886–1905.

Hou, A. Y., and S. Q. Zhang, 2007: Assimilation of precipitation information using column model physics as a weak constraint. *J. Atmos. Sci.,* **64,** 3865–3878.

——, ——, and O. Reale, 2004: Variational continuous assimilation of TMI and SSM/I rain rates: Impact on GEOS-3 hurricane analyses and forecasts. *Mon. Wea. Rev.,* **132,** 2094–2109.

——, G. Skofronick-Jackson, C. D. Kummerow, and J. M. Shepherd, 2008: Global precipitation measurement. *Precipitation: Advances in Measurement, Estimation and Prediction,* S. Michaelides, Ed., Springer, 131–169.

Isaksen, L., J. Haseler, R. Buizza, and M. Leutbecher, 2010: The new ensemble of data assimilations. *ECMWF Newsletter,* No. 123, Reading, United Kingdom, 17–21.

Kleist, D. T., D. Parrish, J. Whitaker, and X. Wang, 2010: Hybrid variational-ensemble data assimilation at NCEP. *Fourth EnKF Workshop,* Rensselaervile, NY, The Pennsylvania State University. [Available online at http://hfip.psu.edu/EDA2010/.]

Kummerow, C., W. S. Olson, and L. Giglio, 1996: A simplified scheme for obtaining precipitation and vertical hydrometeor profiles from passive microwave sensors. *IEEE Trans. Geosci. Remote Sens.,* **34,** 1213–1232.

Lin, X., and A. Y. Hou, 2008: Evaluation of coincident passive microwave rainfall estimates using TRMM PR and ground measurements as references. *J. Appl. Meteor. Climatol.,* **47,** 3170–3187.

Lin, Y., and K. E. Mitchell, 2005: The NCEP stage II/IV hourly precipitation analyses: Development and applications. Preprints, *19th Conf. on Hydrology,* San Diego, CA, Amer. Meteor. Soc., 1.2. [Available online at http://ams.confex.com/ams/pdfpapers/83847.pdf.]

Lopez, P., 2007: Cloud and precipitation parameterizations in modeling and data assimilation: A review. *J. Atmos. Sci.,* **64,** 3766–3784.

Matsui, T., and Coauthors, 2009: Evaluation of long-term cloud-resolving model simulations using satellite radiance observations and multifrequency satellite simulators. *J. Atmos. Oceanic Technol.,* **26,** 1261–1274.

Meng, Z., and F. Zhang, 2008: Tests of an ensemble Kalman filter for mesoscale and regional-scale data assimilation. Part IV: Comparison with 3DVAR in a month-long experiment. *Mon. Wea. Rev.,* **136,** 3672–3682.

——, and ——, 2011: Limited-area ensemble-based data assimilation. *Mon. Wea. Rev.,* **139,** 2025–2045.

Montmerle, T., and L. Berre, 2010: Diagnosis and formulation of heterogeneous background-error covariances at the mesoscale. *Quart. J. Roy. Meteor. Soc.,* **136,** 1408–1420.

Roberts, N. M., and H. W. Lean, 2008: Scale-selective verification of rainfall accumulations from high-resolution forecasts of convective events. *Mon. Wea. Rev.,* **136,** 78–97.

Simpson, J., C. Kummerow, W.-K. Tao, and R. F. Adler, 1996: On the Tropical Rainfall Measuring Mission (TRMM). *Meteor. Atmos. Phys.,* **60,** 19–36.

Tao, W. K., 2003: Goddard Cumulus Ensemble (GCE) model: Application for understanding precipitation processes. *Cloud Systems, Hurricanes and the Tropical Rainfall Measuring Mission (TRMM): A Tribute to Dr. Joanne Simpson, Meteor. Monogr.,* No. 51, Amer. Meteor. Soc., 103–108.

Tarantola, A., 1987: *Inverse Problem Theory and Methods for Model Parameter Estimation.* Elsevier, 352 pp.

Tong, M., and M. Xue, 2008a: Simultaneous estimation of microphysical parameters and atmospheric state with simulated radar data and ensemble square root Kalman filter. Part I: Sensitivity analysis and parameter identifiability. *Mon. Wea. Rev.,* **136,** 1630–1648.

——, and ——, 2008b: Simultaneous estimation of microphysical parameters and atmospheric state with simulated radar data and ensemble square root Kalman filter. Part II: Parameter estimation experiments. *Mon. Wea. Rev.,* **136,** 1649–1668.

Treadon, R. E., H.-L. Pan, W.-S. Wu, Y. Lin, W. S. Olson, and R. J. Kuligowski, 2002: Global and regional moisture analyses at NCEP. *Proc. ECMWF/GEWEX Workshop on Humidity Analysis,* Reading, United Kingdom, European Centre for Medium-Range Weather Forecasts, 33–47.

Whitaker, J. S., T. M. Hamill, X. Wei, Y. Song, and Z. Toth, 2008: Ensemble data assimilation with the NCEP Global Forecast System. *Mon. Wea. Rev.,* **136,** 463–482.

Wilheit, T., C. Kummerow, and R. Ferraro, 2003: Rainfall algorithms for AMSR-E. *IEEE Trans. Geosci. Remote Sens.,* **41,** 204–213.

Yang, S.-C., E. Kalnay, B. Hunt, and N. E. Bowler, 2009: Weight interpolation for efficient data assimilation with the local ensemble transform Kalman filter. *Quart. J. Roy. Meteor. Soc.,* **135,** 251–262.

Zeng, X., W. K. Tao, S. Lang, A. Y. Hou, M. Zhang, and J. Simpson, 2008: On the sensitivity of atmospheric ensemble states to cloud microphysics in long-term cloud-resolving model simulations. *J. Meteor. Soc. Japan,* **86A,** 45–65.

Zupanski, D., S. Q. Zhang, M. Zupanski, A. Y. Hou, and S. H. Cheung, 2011: A prototype WRF-based ensemble data assimilation system for dynamically downscaling satellite precipitation observations. *J. Hydrometeor.,* **12,** 118–134.

Zupanski, M., 2005: Maximum likelihood ensemble filter: Theoretical aspects. *Mon. Wea. Rev.,* **133,** 1710–1726.

——, I. M. Navon, and D. Zupanski, 2008: The maximum likelihood ensemble filter as a non-differentiable minimization algorithm. *Quart. J. Roy. Meteor. Soc.,* **134,** 1039–1050.